

# A preliminary global map of the vector lunar crustal magnetic field based on Lunar Prospector magnetometer data

N. C. Richmond<sup>1,2</sup> and L. L. Hood<sup>1</sup>

Received 3 May 2007; revised 26 July 2007; accepted 24 October 2007; published 26 February 2008.

[1] Previous processing of the Lunar Prospector magnetometer (LP-MAG) data has yielded ~40% coverage of the Moon. Here, new mapping of the low-altitude LP-MAG data is reported with the goal of producing the first global vector map of the lunar crustal magnetic field. By considering all data regardless of the external plasma environment and using less restrictive editing criteria, 2360 partial and complete passes have been identified that can be used to investigate the lunar crustal magnetic anomalies. The cleanest global coverage is provided using 329 low-altitude nightside and terminator passes. An inverse power method has been used to continue the final mapping data to constant altitude. Using the 329 optimal passes, global maps of the lunar crustal magnetic field are constructed at 30 and 40 km. Consistent with previous studies: (1) the largest concentrations of anomalies are mapped antipodal to the Crisium, Serenitatis, Imbrium, and Orientale basins and (2) isolated anomalies at Reiner Gamma, Rima Sirsalis, Descartes, and Airy are mapped. Anomalies previously unmapped by the LP-MAG experiment include (1) isolated anomalies near the craters Abel and Hartwig, (2) weak magnetization within the Nectarian-aged Crisium and Moscoviense basins, and (3) a relatively weak anomaly in an area dominated by crater chains associated with the formation of Nectaris. Future work with the new low-altitude data set is discussed and will include determining whether the lunar anomalies are capable of deflecting the solar wind and investigating directions of magnetization to evaluate a possible former core dynamo.

**Citation:** Richmond, N. C., and L. L. Hood (2008), A preliminary global map of the vector lunar crustal magnetic field based on Lunar Prospector magnetometer data, *J. Geophys. Res.*, 113, E02010, doi:10.1029/2007JE002933.

## 1. Introduction

[2] Analysis of Apollo 15 and 16 subsatellite data [e.g., Coleman *et al.*, 1972; Russell *et al.*, 1975; Hood, 1980; Hood *et al.*, 1981; Lin *et al.*, 1988], results from the Lunar Prospector Electron Reflectometer (LP-ER) experiment [e.g., Lin *et al.*, 1998; Halekas *et al.*, 2001, 2003], and early results from the Lunar Prospector magnetometer (LP-MAG) experiment [e.g., Hood *et al.*, 2001; Richmond *et al.*, 2003, 2005] have yielded information on the distribution and nature of lunar crustal magnetization. The largest concentrations of anomalies have been mapped antipodal to the similarly aged Crisium, Serenitatis, Imbrium, and Orientale basins [Lin *et al.*, 1988; Mitchell *et al.*, 2008]. In addition, a number of isolated anomalies have been mapped, most notably at Reiner Gamma [e.g., Hood, 1980; Hood *et al.*, 2001], Rima Sirsalis [e.g., Hood *et al.*, 2001], Descartes [Halekas *et al.*, 2001; Richmond *et al.*, 2003], and Airy [Hughes *et al.*, 2006].

[3] In general, it has been found that basin ejecta units or other basin-related terranes appear to be magnetized [e.g.,

Strangway *et al.*, 1973; Hood *et al.*, 2001; Halekas *et al.*, 2001; Richmond *et al.*, 2005]. However, while some basin ejecta units are magnetized, the basins themselves are generally characterized by weak fields [e.g., Halekas *et al.*, 2003]. In particular, the weakest fields on the Moon correspond to the Imbrium and Orientale basins [e.g., Halekas *et al.*, 2003], yet large concentrations of strong anomalies have been mapped near the antipodes of those two basins [Lin *et al.*, 1988; Mitchell *et al.*, 2008]. One hypothesis for this intriguing distribution is that an impact-generated plasma cloud produced by the basin-forming impact interacted with a weak magnetic field, expanded around the Moon and produced a compressed, enhanced magnetic field at the basin antipode [Hood and Vickery, 1984; Hood and Huang, 1991; Hood and Artemieva, 2008]. Shock magnetization at the antipode resulting from converging primary impact-generated seismic waves [e.g., Schultz and Gault, 1975] and/or an antipodal concentration of secondary impacting basin ejecta [e.g., Moore *et al.*, 1974] in the presence of the enhanced field could then explain the strong antipode anomalies and lack of basin magnetization (see discussion by Hood and Artemieva [2008]).

[4] An alternative explanation for the magnetization is that it was acquired during one or more relatively recent impacts by cometary comas [Gold and Soter, 1976; Schultz and Srnka, 1980]. One factor behind this explanation is that

<sup>1</sup>Lunar and Planetary Laboratory, University of Arizona, Tucson, Arizona, USA.

<sup>2</sup>Planetary Science Institute, Tucson, Arizona, USA.

high crustal fields appear to correlate with areas of unusual albedo [e.g., Hood, 1980; Richmond *et al.*, 2003; Richmond *et al.*, 2005; Hughes *et al.*, 2006]. It has been suggested that the high albedo is due to recent surface scouring by a cometary coma, with the magnetization resulting from the interaction of fields in the cometary coma with the lunar regolith. In this interpretation, the concentration of anomalies antipodal to similarly aged basins is considered fortuitous. Surface scouring by a recent micrometeoroid impact has also been proposed [Starukhina and Shkuratov, 2004]. This explanation again argues that the location of the anomaly clusters antipodal to similarly aged basins is fortuitous and initially this proposal was limited due to an inability to explain the association between albedo and magnetization. However, recent refinements of this mechanism suggest that the magnetization could be due to compression of the interplanetary magnetic field resulting from the simultaneous impact of a number of meteoroids in close proximity to each other [Starukhina, 2007].

[5] On the other hand, the unusual albedo could be the result of the interaction between preexisting crustal magnetization and the incident solar wind. Numerical models [e.g., Harnett and Winglee, 2003] have indicated that the lunar crustal anomalies may be capable of deflecting the solar wind. Micrometeoroid impacts and solar wind ion bombardment [e.g., Housley, 1977; Pieters *et al.*, 1993; Taylor *et al.*, 2001] have been proposed as possible mechanisms behind the optical maturation, or darkening, of the lunar regolith. However, it is uncertain whether both processes are required. If the crustal anomalies are able to deflect the solar wind, then the high albedo may be due to the anomalies shielding the regolith [Hood and Schubert, 1980; Hood and Williams, 1989; Richmond *et al.*, 2003], which may indicate that solar wind ion bombardment is a necessary and sufficient process behind at least part of the optical maturation of the lunar regolith. Kurata *et al.* [2005] and Nicholas *et al.* [2007] have argued for the existence of a minimagnetosphere at Reiner Gamma, which provides further evidence in support of the magnetic shielding hypothesis.

[6] This uncertainty regarding the origin of the magnetic anomalies restricts the application of lunar magnetism to the study of other geophysical properties. For example, it is currently uncertain whether a core dynamo existed during early lunar history. The existence of a core dynamo field, or the lack thereof, has implications for the thermal history of the Moon [e.g., Stegman *et al.*, 2003]. As mentioned previously, some basins are characterized by very weak fields (e.g., Imbrium and Orientale). However, weak but measurable basin magnetization has been identified in the LP-ER data for a number of large, old basins [Halekas *et al.*, 2003]. It has been suggested that the results may support the existence of a core dynamo during the Nectarian period, though that is not certain. However, as discussed before, the strongest crustal fields are located antipodal to four similarly aged Nectarian/Lower Imbrian basins (using the dating of Wilhelms [1987]). Statistical and theoretical analyses have argued that those anomalies are associated with the formation of the basins [e.g., Richmond *et al.*, 2005; Hood and Artemieva, 2008] and do not necessarily require the existence of a core dynamo field strong enough to cause the magnetization. Further, paleointensity results from returned

lunar samples [Fuller and Cisowski, 1987] indicate that fields were high in both the Nectarian and early Imbrian times, a result that is not fully supported by the LP-ER data [Halekas *et al.*, 2003]. As a result, it is currently uncertain whether a core dynamo field is required to explain the crustal magnetization.

[7] It is clear that despite studies using the available data, the nature of the magnetizing field, the source materials, and the way in which the anomalies interact with the solar wind remain only partially understood. The new global LP-ER record [Mitchell *et al.*, 2008] is a valuable source of information on the distribution of magnetization, but it has limitations. In particular, it does not provide directional information, which is essential if the nature of the crustal sources and the origin of the magnetizing field(s) are to be understood. The ER data are well suited to characterizing weaker fields, particularly those due to near-surface sources. In contrast, the LP-MAG data are acquired at finite altitudes above the surface and are therefore more sensitive to deeper sources and strong fields.

[8] In this study, we revisit the processing and mapping of the LP-MAG data with the goal of producing the first global vector coverage of the crustal magnetization. The revised data analysis is described in section 2. The altitude continuation and mapping are discussed in section 3. A global map of the field magnitude and the key features presented are discussed in section 4. A summary of the main results and future work is given in section 5.

## 2. Data Analysis

[9] Lunar Prospector was launched in January 1998 into a high-altitude ( $\sim 100$  km) polar lunar orbit chosen for optimum compositional mapping. During the extended phase of the mission (January–July 1999), the spacecraft altitude was lowered to  $\sim 15$ – $45$  km to provide improved coverage for mapping the magnetic and gravity fields. It is the low-altitude data from 1999 that we consider here.

[10] Previous processing and analysis of the LP-MAG data have been carried out, which provided coverage of only approximately 40% of the Moon (see Figure 1) [Hood *et al.*, 2001; Richmond *et al.*, 2005]. This limited coverage is due to the data selection and strict editing criteria which was intended to minimize external field contributions. The method used in this study follows directly from those studies, but we modify it to obtain extended coverage. In the following sections, the main steps of the processing are described, with emphasis on the differences from previous work.

### 2.1. Data Selection

[11] Previous analysis of the LP-MAG data [Hood *et al.*, 2001] restricted the data selection by using only passes when the Moon was in the geomagnetic tail lobes or when the Moon was in the solar wind, but the spacecraft was in the lunar wake (see Figure 2). While it is true that these represent the quietest external plasma conditions, there are two disadvantages to this selection approach. First, other plasma conditions are more likely to be contaminated by external fields, but some usable data may remain. In addition, even if some external fields remain in the data, those passes may still be useful for putting limits on the

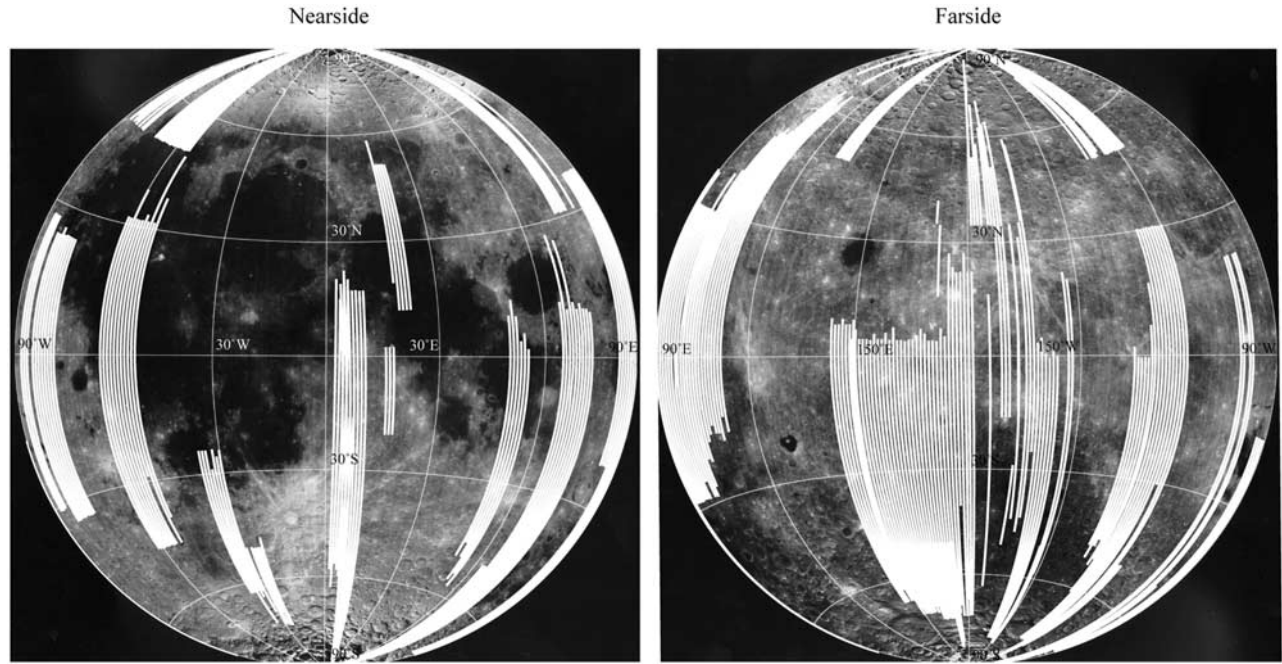


**Figure 1.** Orbit tracks for the coverage obtained from previous analysis of the LP-MAG data [Hood *et al.*, 2001; Richmond *et al.*, 2005], presented using a Lambert equal area projection. In some areas, for example, 150–180°E at 60°S, multiple sets of passes were obtained. The background image is the Clementine albedo map.

magnitude of the crustal anomalies. If no clear passes are available over a particular location, it is better to have a limit on the strength of the crustal sources from the available passes rather than no information at all. While this will provide an upper limit for the magnitude of any possible crustal sources, the crustal field strength could have a value from 0 nT up to the upper limit provided by the solar wind measurements, and thus these passes do not provide quantitative information on the nature of crustal sources. In addition, many passes will be affected by external fields of the order of tens of nT. Such passes cannot be used to obtain any meaningful information on the upper limit for possible crustal sources. Therefore it is highly desirable to have coverage for all areas that is free of external field contamination and this will be discussed further in section 3.

[12] Second, Kurata *et al.* [2005] reported the existence of a minimagnetosphere over Reiner Gamma, which was determined by comparing LP-MAG data over the anomaly during different plasma conditions. Consequently, by analyzing all passes for a range of plasma conditions, it may be possible to use the resulting data set to determine whether any or all of the crustal anomalies are strong enough to deflect the solar wind and create minimagnetospheres. This will be discussed in section 4.5.

[13] Therefore, in this study we consider initially all low-altitude data, regardless of the location of the Moon relative to the Earth's magnetosphere or the location of the spacecraft relative to the Moon.

## 2.2. Data Processing

[14] The main processing approach applied to the selected data follows directly from Hood *et al.* [2001] and Richmond *et al.* [2005]. First, the data are converted to a lunar centered

radial, east and north coordinate system. At this stage all passes are catalogued according to whether (1) the spacecraft is on the nightside, dayside or terminator of the Moon and (2) whether the Moon is in the magnetotail, magnetosheath or exposed to the solar wind (see Table 1).

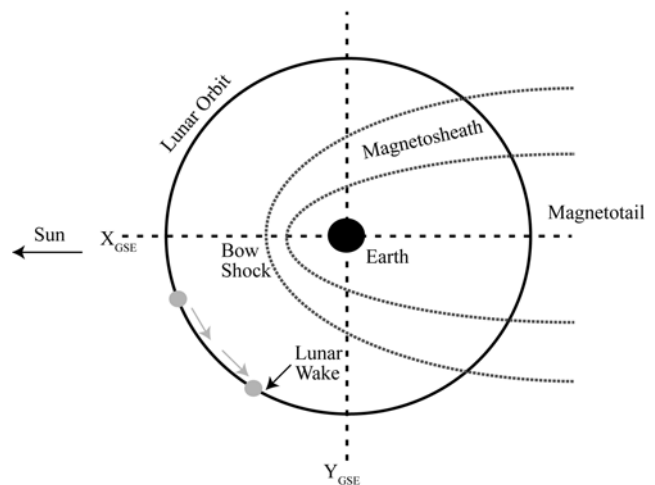


**Figure 2.** Lunar position for passes 241–280 from January 1999. During each month the Moon passes through the magnetotail, magnetosheath, and solar wind outside the magnetosphere. The axes on the plot are given in Geomagnetic Solar Ecliptic coordinates. In this system, the  $x$  axis is aligned with the Sun-Earth line (positive from the Earth toward the Sun) and the  $y$  axis lies within the ecliptic plane, positive pointing toward dusk. The  $z$  axis (not shown) points to the ecliptic north pole.



**Table 1.** Number of Passes Under Different Plasma Conditions for Each Month of the Low-Altitude Phase of the LP-MAG Experiment<sup>a</sup>

Month	Total Number of Passes	Solar Wind (D-N-T)	Magnetosheath (D-N-T)	Magnetotail (D-N-T)
January	795	201-202-156	29-28-64	23-23-69
February	707	266-265-0	64-65-0	24-23-0
March	793	271-271-0	65-64-0	61-61-0
April	764	266-266-0	71-71-0	45-45-0
May	801	266-265-0	70-72-0	66-64-0
June	778	264-263-0	46-47-59	4-3-92
July	740	53-55-428	32-33-66	37-36-0

<sup>a</sup>D, dayside; N, nightside; T, terminator.

[15] In order to remove long-wavelength external fields, a low-order polynomial was then fitted and removed from each component of each orbit. Figure 3 compares the radial component from a series of passes over Reiner Gamma and Rima Sirsalis (299.4–307.6°E) from July 1999, shown before and after removal of long-period external fields. Long-period signals are clear in the passes prior to detrending, but they are effectively removed by the detrending process [see also *Hood et al.*, 1981]. For the north component, it was found that some long-period external fields remained over the Northern Hemisphere, with field strengths up to  $\sim 2$  nT. These remaining external fields were removed by fitting and removing a polynomial from the Northern and Southern hemispheres individually. While the north component was most badly affected, this was done for all three components.

### 2.3. Removing Short-Period External Fields

[16] The final stage of processing is the removal of remaining short-period external fields. This is done by visually examining all passes and identifying measurements that do not repeat on adjacent passes. In the previous mapping [*Hood et al.*, 2001; *Richmond et al.*, 2005], very strict criteria were used. While there are clear advantages to such an approach, it will limit the final data available. The goal of this study is to produce an acceptably accurate map with maximum possible coverage. In the interest of obtaining as much data as possible under all plasma conditions, less restrictive criteria are therefore most useful. Figure 4 presents the total field and radial, north and east field components for a series of passes over the east side of the Moon. The quality of these data is typical of the final processed LP-MAG data. It is clear that, in general, both long- and short-period external fields have been successfully removed. Two crustal sources are shown in Figure 4: the Orientale antipode group ( $\sim 15^\circ$ N) and an isolated anomaly near Abel ( $\sim 30^\circ$ S). For all passes, the crustal sources are clearly identifiable by their repetition on successive passes. The external fields (i.e., the signals that do not repeat on adjacent passes) are lower in strength than  $\sim 2$  nT, which is significantly lower than the magnitude of the crustal sources.

### 2.4. Comparisons With Alternate Mapping Techniques

[17] *Purucker et al.* [2006] have reported an alternate method for minimizing external field contributions to Lunar

Prospector magnetometer data. Basically, a model of the external field was developed for periods when the Moon was in the geomagnetic tail. The external field was assumed to be uniform, which is a good approximation in the geotail.

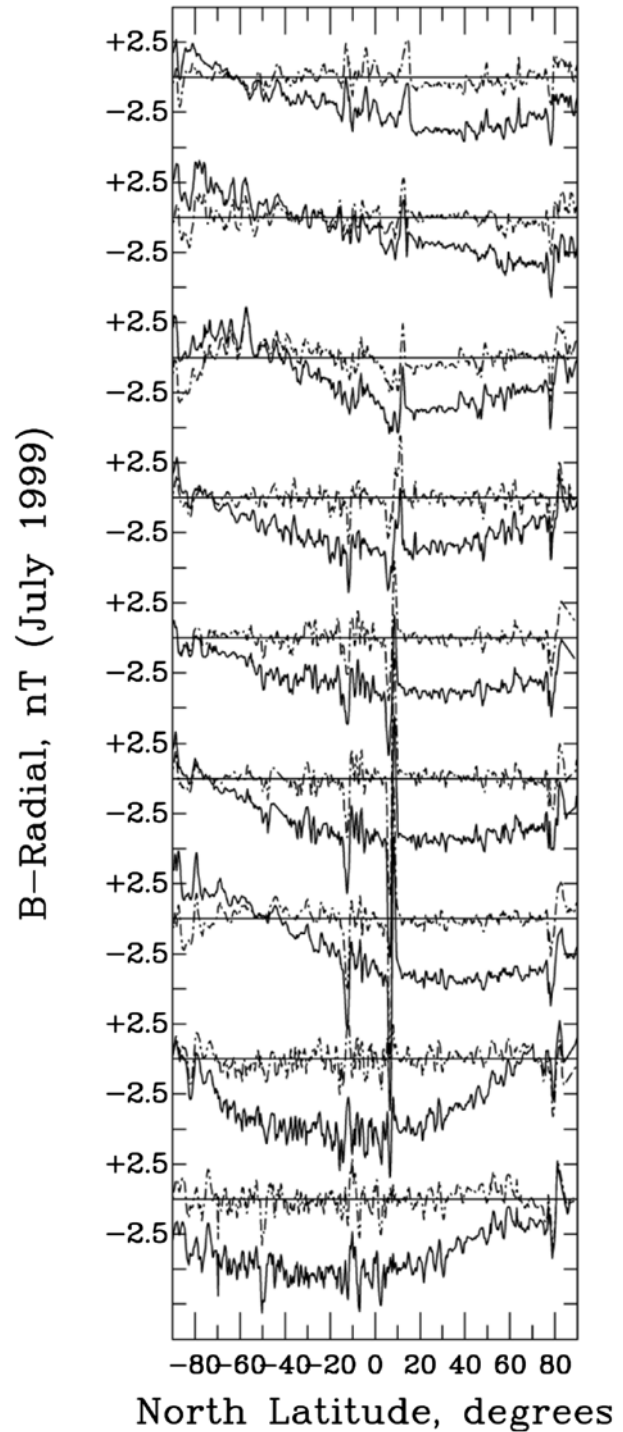


**Figure 3.** Passes 116–124 from July 1999 comparing the data before (solid) and after (dotted) detrending. The passes cover longitudes (top) 299.4°E to (bottom) 307.6°E. The anomalies shown in the data just north and just south of the lunar equator are Reiner Gamma and Rima Sirsalis, respectively.

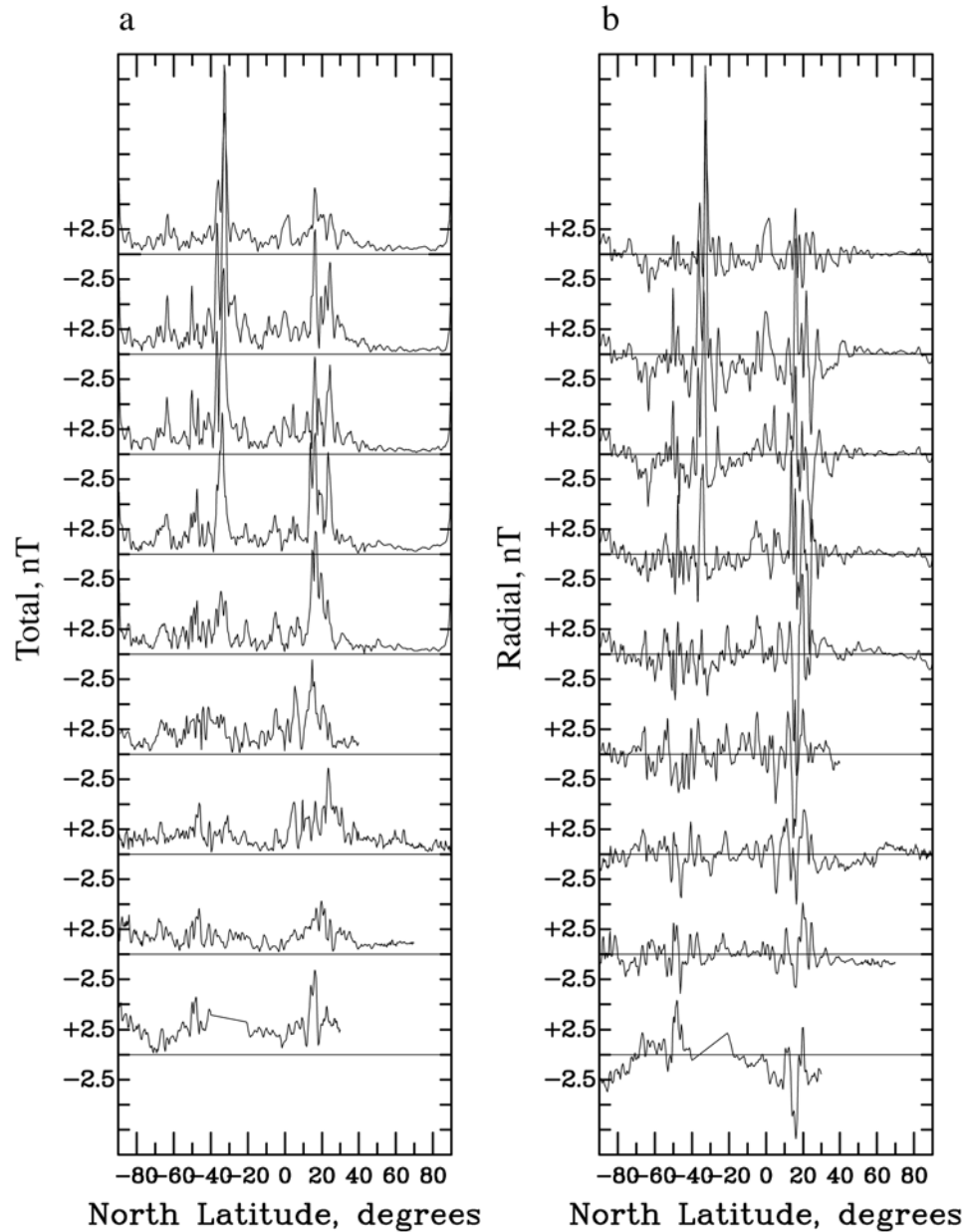


**Figure 4.** Example final passes from 87.2 to 95.3°E, following processing and examination for remaining external fields. Shown are the (a) total field and (b) radial, (c) north and (d) east components. The strong anomalies at ~15°N are the Orientale antipode group located near Mare Marginis. The strongest anomaly shown is the isolated anomaly located near the crater Abel (~30°S), between Humboldt and Mare Australe.

After subtracting the external field model from the field component data, the residuals were examined and only those passes were retained that showed good pass-to-pass coherence of field patterns. This approach differs from our method mainly in the use of the external field model, rather than quadratic detrending, to minimize long-wavelength external fields. It has an advantage in that it treats the external field as a potential field. On the other hand, the quadratic detrending method may be more effective in removing temporally varying external fields, which are often present even in the geotail. In any case, exchanges of processed data over the South Pole–Aitken region

(M. Purucker, private communication, 2006) verifies that crustal field maps produced using the external field model method and the quadratic detrending method are nearly identical.

### 3. Global Mapping

#### 3.1. Data Obtained Under Different Plasma Conditions

[18] Using the method described in section 2, 2360 complete or partial low-altitude passes have been identified as being sufficiently low in external field contamination to be usable for investigating the nature and origin of lunar crustal magnetization. Table 2 lists the number of relatively

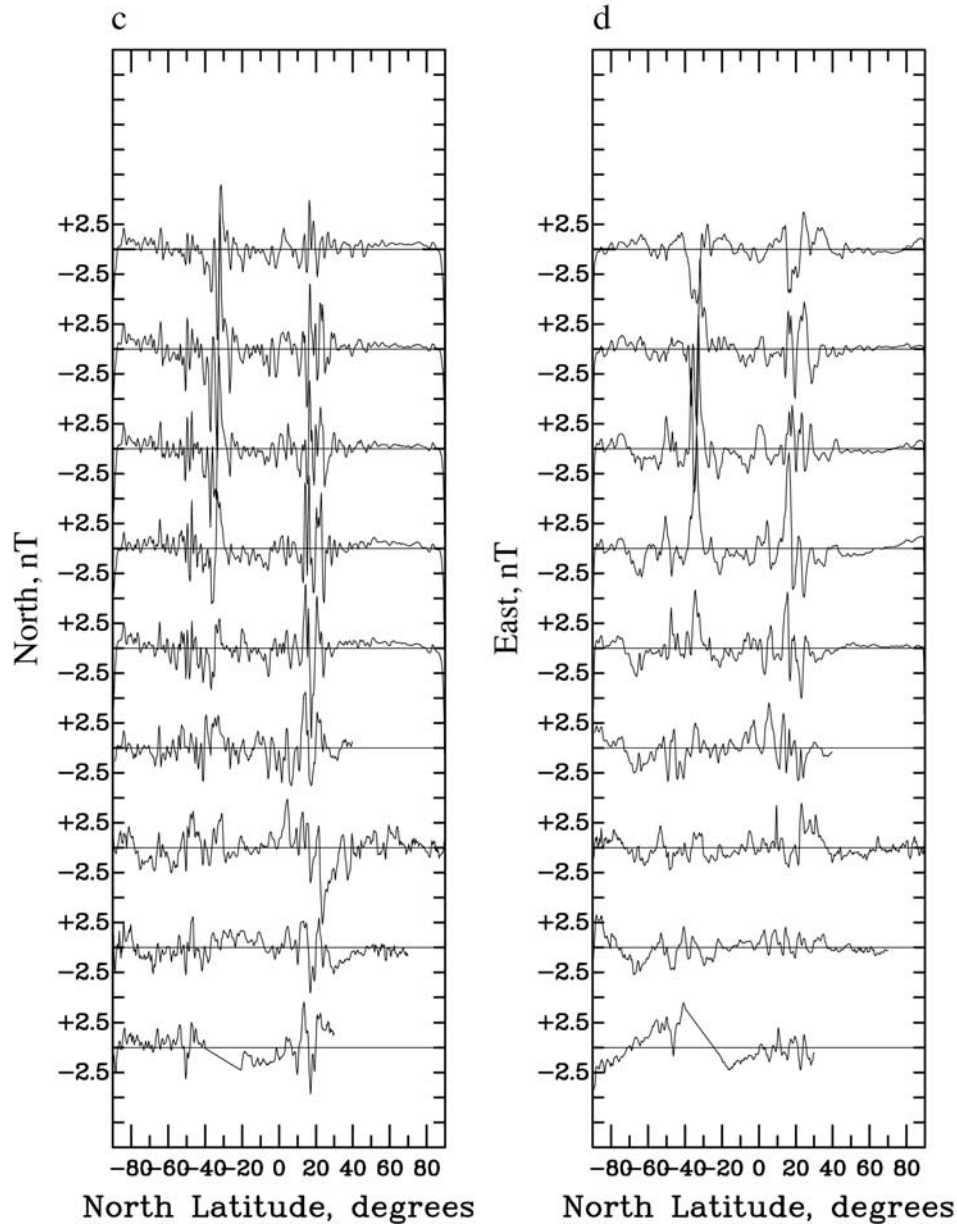


Figure 4. (continued)

clean passes for each month as a function of lunar position and spacecraft position. As would be expected, nightside data and measurement when the Moon was in the geomagnetic tail were the quietest. As will be shown below, these data are still the best for constructing global maps of the permanent crustal field. However, some usable data were found for other conditions. While many usable passes have been identified from the dayside, when the Moon was in the solar wind, the remaining external fields in these data are higher than in the nightside passes. However, the external fields are below  $\sim 3$  nT for all passes identified using the method in section 2. It is noted that, depending upon the external conditions, the measurements may be affected by the plasma environment regardless of the processing carried out here. These effects must be considered in selecting data

for a global map and before the data can be used to study the directions of magnetization or other quantitative analysis.

### 3.1.1. Quiet Plasma Conditions

[19] Passes when Lunar Prospector was in the lunar wake or in the geomagnetic tail region (see Figure 2) provide measurements of the crustal sources under magnetically quiet external conditions. While there are large-scale fields in the tail region, these are straightforward to remove using the polynomial detrending method described previously. In the lunar wake, external fields are minimal as the Moon shelters the nightside from the solar wind ion bombardment.

[20] Measurements when Lunar Prospector was in magnetically quiet plasma conditions represent the highest-quality data, when external fields are either largely absent (see 3.1.3 below) or straightforward to remove. The high

**Table 2.** Clean Complete and Partial Passes Identified Following Data Processing<sup>a</sup>

Month	Total Number of Clean Passes	Solar Wind (D-N-T)	Magnetosheath (D-N-T)	Magnetotail (D-N-T)
January	301	85-87-73	0-6-23	4-13-10
February	268	105-117-0	4-11-0	17-14-0
March	430	163-175-0	4-20-0	26-42-0
April	423	130-179-0	26-38-0	21-29-0
May	342	113-129-0	8-36-0	26-30-0
June	220	143-34-0	3-0-7	0-0-33
July	376	15-13-265	7-8-14	27-27-0

<sup>a</sup>D, dayside; N, nightside; T, terminator.

signal-to-noise ratio makes these data ideal for mapping the distribution of crustal anomalies and of sufficiently high quality for the calculation of quantitative estimates of source properties, such as directions of magnetization.

### 3.1.2. Magnetosheath Passes

[21] The magnetosheath is a complex magnetic boundary layer between the magnetosphere, in which the geomagnetic field dominates, and the interplanetary magnetic field, which is carried by the solar wind (see Figure 2). As such, it is a region dominated by rapidly varying fields that can be of large magnitude. In this study, we consider the magnetosheath to be static, extending from  $130^{\circ}\text{E}_{\text{GSE}}$  and  $200^{\circ}\text{E}_{\text{GSE}}$ , where GSE are Geomagnetic Solar Ecliptic coordinates. In this system, the  $x$  axis is aligned with the Sun-Earth line (positive from the Earth toward the Sun) and the  $y$  axis lies within the ecliptic plane, positive pointing toward dusk. In general, these passes are of limited use in studying the crustal magnetic field, due to the large and variable external fields. However, some usable data categorized as magnetosheath passes in this study have been obtained, primarily as a result of the variation of the location of the magnetosheath as a function of solar wind conditions.

### 3.1.3. Terminator Passes

[22] Terminator passes are those within  $\pm 10^{\circ}\text{E}_{\text{GSE}}$  of lunar dawn and dusk. Studies using the electron reflectometer data have identified a wake boundary signal [Halekas *et al.*, 2005], which is collocated primarily with the nightside terminator passes over all latitudes from  $\sim 75^{\circ}\text{N}$  to  $\sim 75^{\circ}\text{S}$ , but is also present across the nightside at about  $75^{\circ}\text{N}$  and  $75^{\circ}\text{S}$ . This signal is stronger than the crustal sources at high altitude, but its effect is less significant relative to the crustal anomalies at the altitudes of the LP-MAG data used in this study [Halekas *et al.*, 2005]. The presence of the wake boundary signal can be identified by comparing passes under different conditions, over the same areas. Consequently, while the wake boundary signal must be considered, it can be identified and removed by comparing multiple sets of coverage over the same areas.

### 3.1.4. Dayside, Solar Wind Passes

[23] Under these conditions, the spacecraft measures both the crustal sources and the interplanetary magnetic field (IMF). The IMF has been removed in this study by visual editing of the data, as external solar wind sources do not repeat on adjacent passes. In addition, comparison of measurements over the same regions obtained in different months and under different plasma conditions, can be used to identify transient fields of solar origin.

[24] However, solar wind effects will remain. It has been shown [e.g., Harnett and Winglee, 2003; Kurata *et al.*, 2005] that the interaction between the solar wind and the crustal anomalies could result in the modification of the field measured for a given anomaly. Results of numerical simulations have indicated that the interaction between the solar wind and crustal anomalies can cause field amplifications and modification of the direction of magnetization [Harnett and Winglee, 2003]. Thus, while dayside solar wind passes can be used to map the general location of crustal sources, they do not provide an accurate measure of the location or strength. These passes cannot be used for the quantitative analysis of lunar crustal sources and could, for example, yield misleading estimates of magnetization direction. Consequently, it is preferable to construct a global map that does not use data obtained under dayside solar wind conditions. However, there are useful applications of these data, which will be discussed in section 4.5.

### 3.1.5. Other Possible External Sources

[25] A number of studies have identified other possible external sources, including the presence of electromagnetic waves associated with the lunar wake [e.g., Nakagawa *et al.*, 2003] or magnetic enhancements associated with strong crustal anomalies [Halekas *et al.*, 2006]. These signals are associated with particular lunar local times or are dependent on solar wind conditions. Consequently, they can be removed by comparing coverage of the same areas obtained under different external plasma conditions.

## 3.2. Data Coverage

[26] For the purpose of constructing a map of the permanent crustal field, the passes remaining after the analysis in section 2 (Table 2) have been examined to identify the cleanest data for each region of the Moon. The best coverage, with the lowest contamination by external fields, was found using the 329 passes listed in Table 3 and represented in Figure 5. These passes are from March, April, May, and July. The passes from March, April and May are primarily nightside data obtained when the Moon was in the solar wind or geomagnetic tail. These are high-quality data from quiet external conditions, which can be used for quantitative study of the lunar anomalies. The July passes are primarily terminator passes when the spacecraft was in the solar wind or geomagnetic tail. Note that the 2360 passes identified in section 2 provide multiple sets of coverage over all regions of the Moon. As a result, it is possible to compare coverage of the same areas under multiple sets of external plasma conditions. The passes indicated in Figure 5 show features that repeat in different months, under different plasma conditions. Therefore we

**Table 3.** Clean Complete and Partial Passes Used to Construct the Global Map Presented in Figure 7<sup>a</sup>

Month	Total Number of Clean Passes	Solar Wind (D-N-T)	Magnetosheath (D-N-T)	Magnetotail (D-N-T)
March	34	0-34-0	0-0-0	0-0-0
April	80	0-62-0	0-1-0	0-17-0
May	94	0-52-0	0-15-0	0-27-0
July	121	0-0-93	7-0-0	21-0-0

<sup>a</sup>D, dayside; N, nightside; T, terminator.



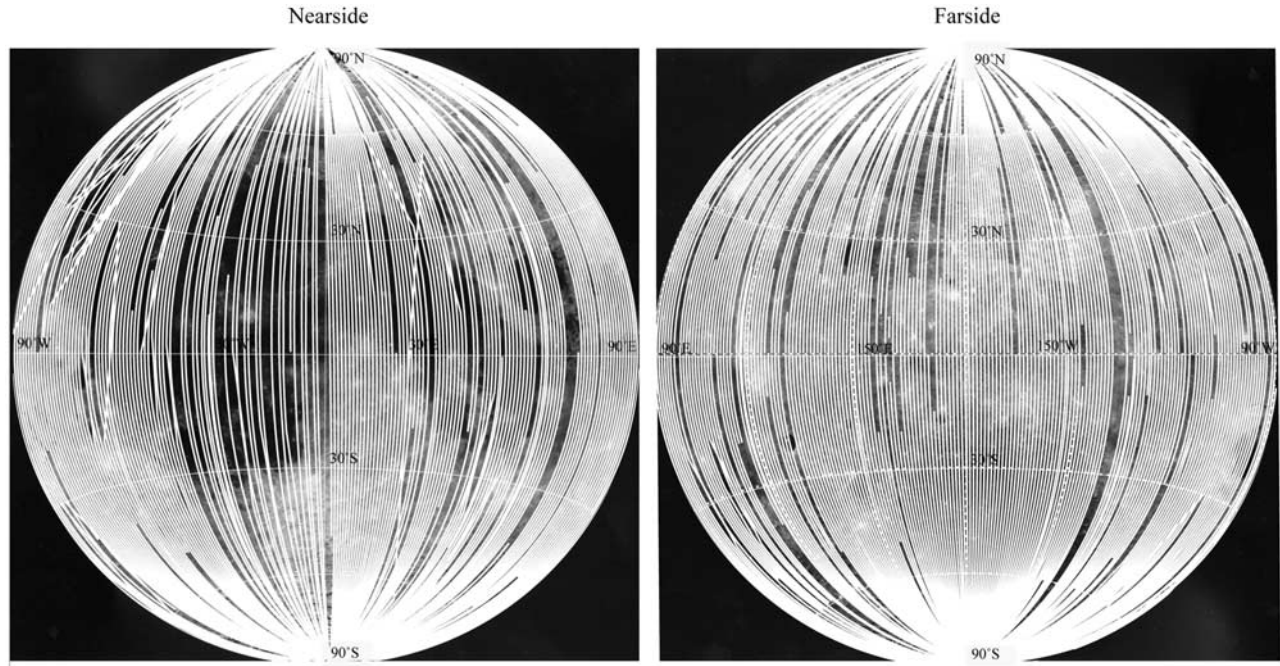


**Figure 5.** Orbit tracks for the 329 clean passes used to produce the global map. The background image is the Clementine albedo map, and the projection used is a Lambert equal-area projection. Linear features that do not follow the curvature of the projection are due to gaps in the data.

believe the measurements used here represent genuine crustal sources. This is particularly important for the terminator passes. We have chosen these data because they provide the best coverage and least variation of altitude. However, in all cases, we have compared the terminator passes with partial coverage that is available from nightside data when the Moon was in the solar wind or geomagnetic tail data. The sources identified in the terminator passes are fully consistent with the available nightside and tail data, and thus we believe the use of terminator data is valid for these passes. In addition, a small number of passes from April, May, and July are categorized as magnetosheath passes in Table 3. We consider the magnetosheath to be static, but in reality the location of this region varies as a function of solar wind conditions. The passes listed as magnetosheath in Table 3 are on the edge of the static limits used in this study and in reality are geomagnetic tail data (April, May, July) and nightside solar wind data (May).

[27] Finally, we stress that the data used in the global map does not use any dayside solar wind data, so it is not affected by inaccuracies in the mapped field magnitudes resulting from the interaction between the solar wind and crustal sources. Thus the pass data used to produce the global map can be used for detailed analysis of the lunar anomalies.

[28] Two small gaps in coverage remain, at  $\sim 70^\circ\text{E}$  and  $\sim 220^\circ\text{E}$ . Coverage of those areas exists in the clean data set; however the altitudes of those passes are significantly different from those of adjacent passes. In selecting the data for the global map, pass selection is a trade-off between the remaining external fields in the data and the altitude of the passes. External fields present an obvious problem and altitude issues will be discussed in section 3.3. To minimize the variation in altitude, gaps remain at those two locations.

[29] Coverage in the global data set is limited over the area from  $\sim 330$  to  $360^\circ\text{E}$ . Unfortunately, for all months and all plasma conditions continuous coverage from adjacent passes (i.e., passes with similar altitudes) were not available for that area. The data that are available for different months indicate that no strong crustal sources are present in the area. Thus the limited coverage over this area is not considered problematic.

### 3.3. Altitude Continuation

[30] A number of different methods are available for the altitude continuation of magnetometer data [e.g., *Purucker et al.*, 1996]. In this study we use the inverse power method that has previously been applied to the LP-MAG data (for a more detailed description, see *Richmond et al.* [2005]):

$$B_z = \frac{B_v}{(Z/V)^X}$$

where  $B_z$  is the radial, north or east field component at constant altitude  $Z$  (in km),  $B_v$  is the field at variable spacecraft altitude  $V$  (in km), and  $X$  is a constant. There are two ways this method can be implemented, either using a site-specific value for  $X$  or a globally averaged value. For the maps presented here we use  $X = 1.5$ . This is an average value estimated by taking two sets of low-altitude LP-MAG data over strong anomalies at two altitudes. The value of  $X$  was varied for each area until the lowest-altitude data could be upward continued to higher altitude and successfully reproduce the magnitude of the anomalies in the higher-altitude LP-MAG measurements. Some variation was found between different areas and the different values of  $X$  have been averaged to obtain the value used in this study. It is



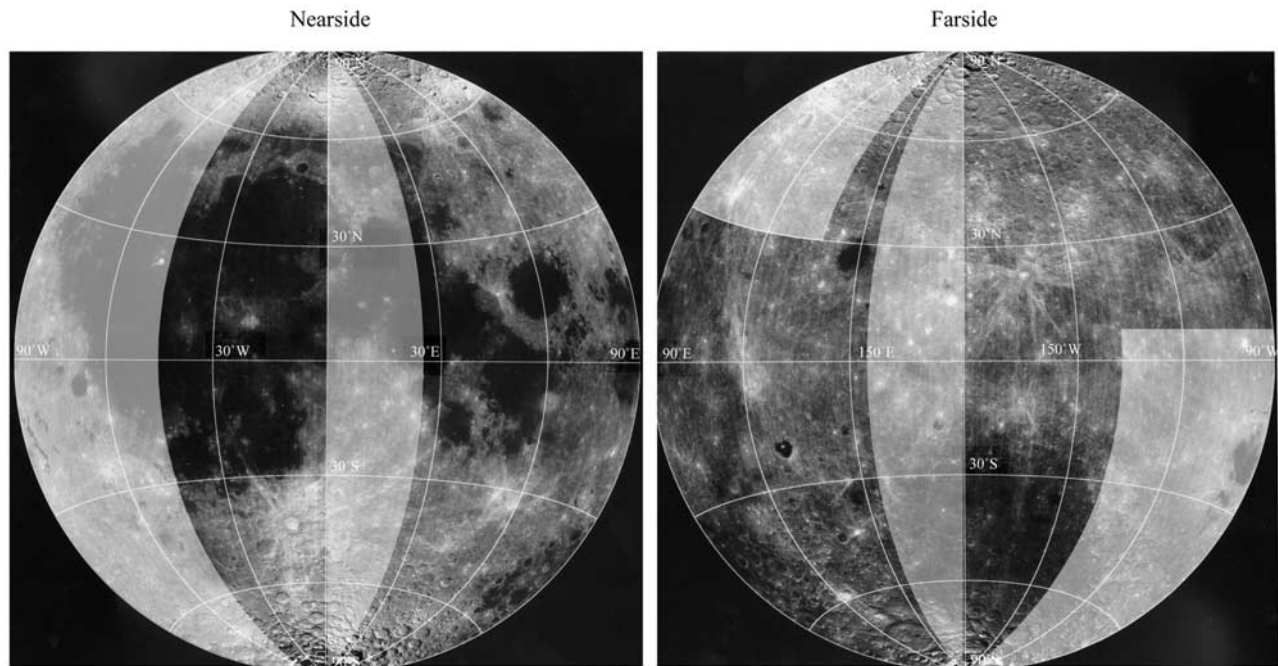


**Figure 6.** Regions for which the passes in Figure 5 are at an altitude of greater than 30 km (shaded grey). Other passes are at less than 20 km (nearside) and 20–30 km (farside). The projection used is a Lambert equal-area projection, and the background image is the Clementine albedo map.

notable that the variation in  $X$  for different areas has applications to the study of the coherence scale of the crustal sources. Future work using this data set will estimate the global variation of  $X$  to investigate regional variations in magnetic coherence. As the goal here is to present the global field, an average value of  $X$  is most appropriate.

### 3.4. Global Constant Altitude Map

[31] The global coverage (Table 3 and Figure 5) was obtained at variable spacecraft altitude. The nearside data prior to continuation are at an altitude of less than 20 km, while the farside data are generally at higher altitude, in the range 20–30 km. The exceptions to this are shown in Figure 6, which shows the areas for which coverage was over 30 km. Using the method described in section 3.3, the radial, north, and east components for each pass have been continued to constant altitude. Following continuation, the data have been filtered two-dimensionally using a moving boxcar algorithm to produce a gridded data set suitable for contour plotting the lunar magnetization. This has been done to produce constant altitude maps at 5 km intervals from 25 to 50 km.

[32] For the lowest-altitude maps this means that some regions have been downward continued. This is problematic as downward continuing increases the magnitude of the contaminating fields, as well as the signal. However, for the study of individual regions, lower-altitude maps are useful, particularly for the nearside where most of the data was obtained at altitudes less than 20 km. The larger the distance over which the upward continuation is carried out, the larger the potential differences between the actual measurements at a given altitude and the upward continued values. The altitude of the original data must be considered when evaluating the reliability of the constant altitude maps,

and the greater the change in altitude the less reliable the results. Therefore, for detailed numerical analysis, the original pass data must be used or data that have been continued over only very short distances.

[33] In the present study, we are interested in the global distribution of magnetization. Therefore we present the constant altitude maps at 30 km and 40 km (Figure 7), which provide global results with a minimum of correction by the altitude continuation process. (High-resolution versions of the total field maps are available (1) in the auxiliary material<sup>1</sup>, (2) from the author's Web site at <http://www.lpl.arizona.edu/~nic/Moon/LPMAG.html>; and (3) from the PSD at <http://pds.jpl.nasa.gov/> (maps submitted to the Planetary Data System (PDS), 2007).) For the 30 km map, the regions shown in Figure 6 have been downward continued. Figure 7 presents the strongest crustal fields mapped, that is, those with smoothed (two-dimensionally filtered) magnitudes over 3 nT. This cutoff has been selected to ensure the maps are free of noncrustal fields, but it is worth noting that for many areas of the Moon, anomalies of lower magnitude can be reliably mapped in this data set. Finally, it should be emphasized that actual field magnitudes at 30 km over certain anomalies (e.g., Reiner Gamma) are locally larger (>10 nT) than the smoothed amplitudes plotted here. Figure 7 presents details on the global distribution of crustal anomalies, but for detailed quantitative analysis, the original data from the passes listed in Table 3 and shown in Figure 5 must be used.

[34] Figure 8 presents the radial, north and east components for the 30 km constant altitude map, using a contour

<sup>1</sup>Auxiliary materials are available in the HTML. doi:10.1029/2007JE002933.

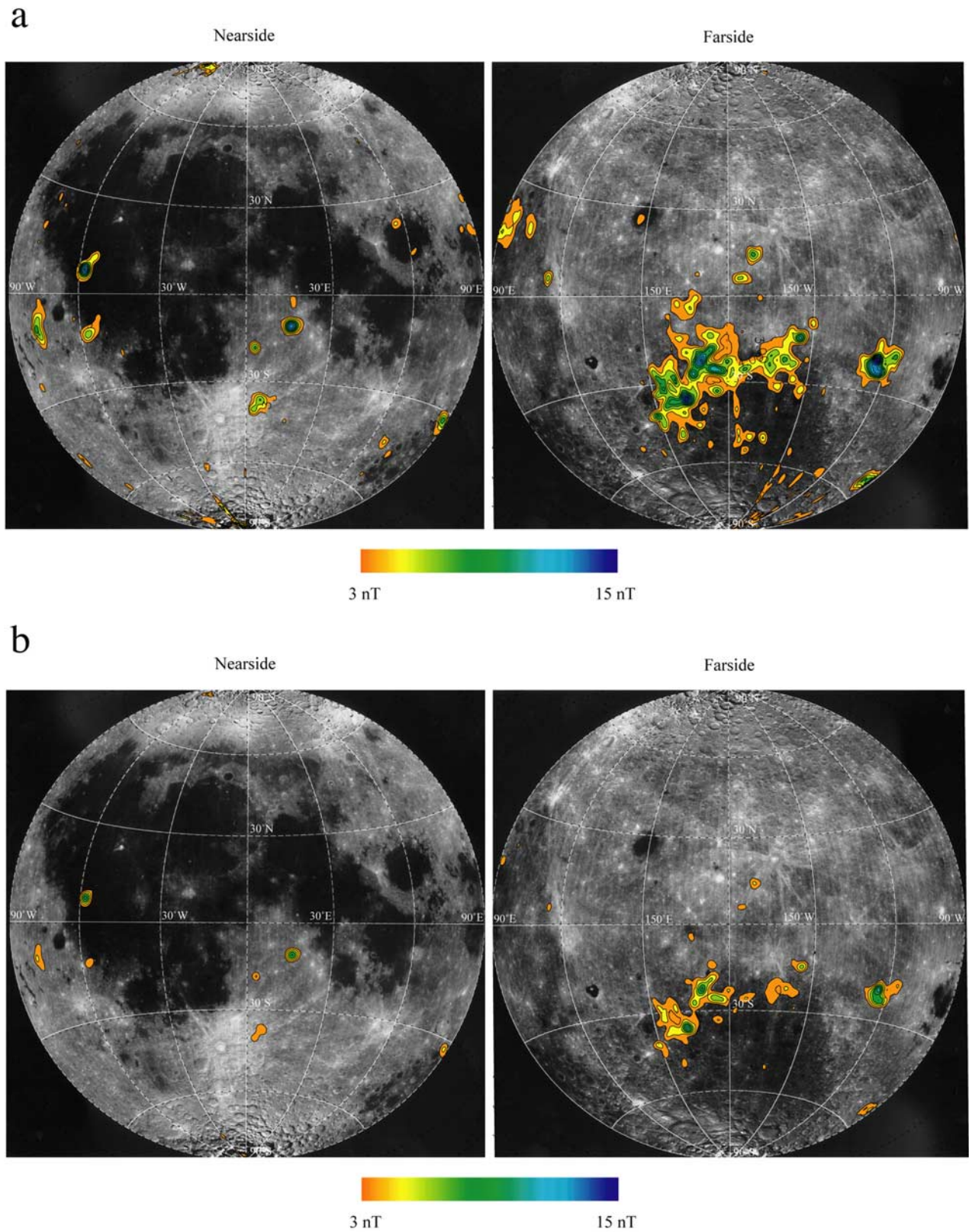


**Figure 7.** Preliminary global map of the total field at a constant altitude of (a) 30 km and (b) 40 km, plotted using a Lambert equal-area projection. The background image is the Clementine albedo map.



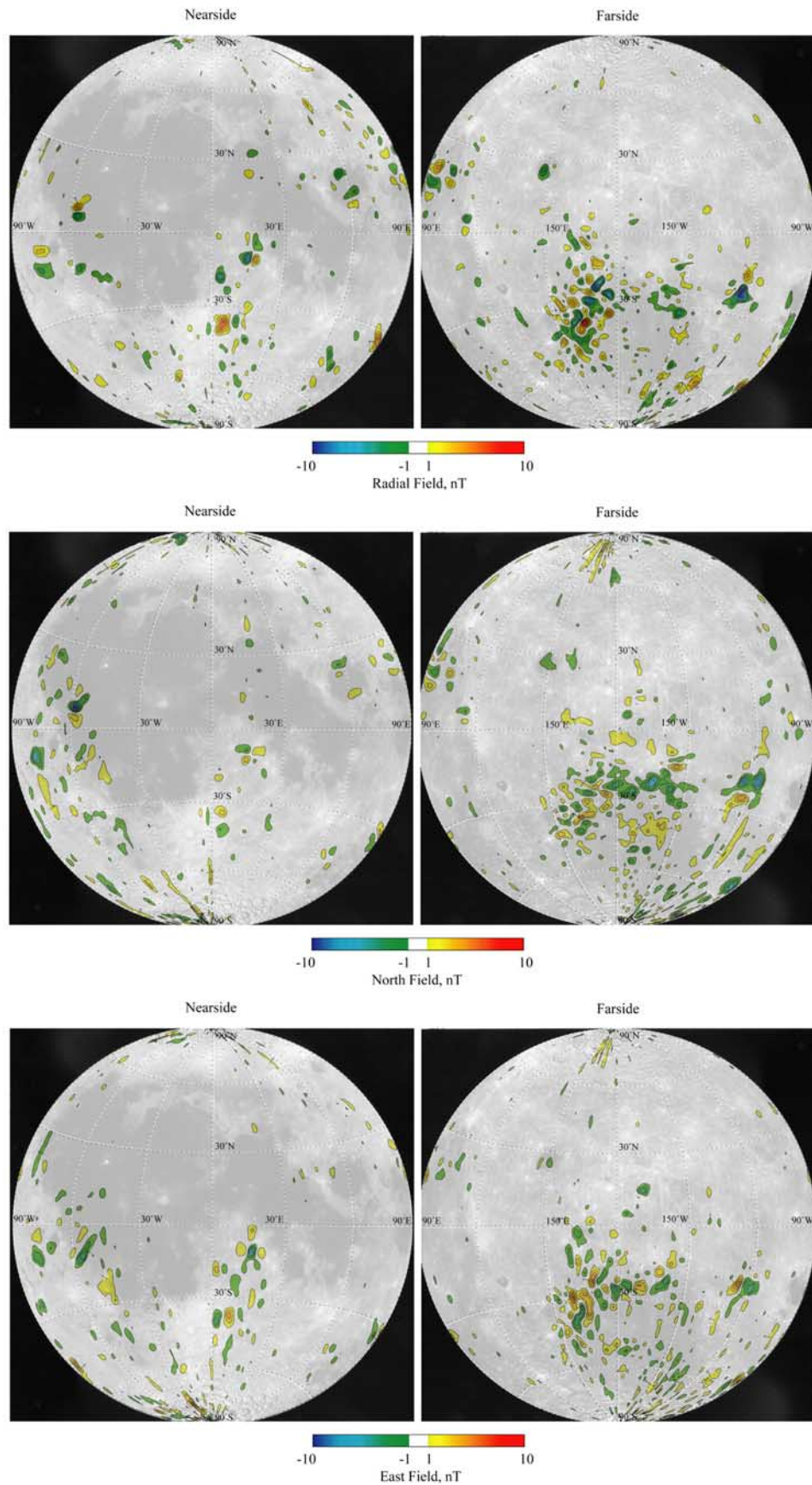


**Figure 8.** (top) Radial, (middle) north, and (bottom) east field components at 30 km altitude, plotted using a Lambert equal-area projection. The contour interval is 1 nT, and the 0 nT contour is not shown.



interval of 1 nT (excluding the 0 nT contour). (High-resolution versions of the component maps are available (1) in the auxiliary material; (2) from the author's Web site at <http://www.lpl.arizona.edu/~nic/Moon/LPMAG.html>; and (3) from the PSD at <http://pds.jpl.nasa.gov/> (maps submitted to the PDS, 2007).) It is clear from Figure 8 that some low-magnitude external fields remain. The north component, in particular, is affected by external fields, though in most cases the contamination is lower than  $\pm 2$  nT. For all three components, the magnitude of the smoothed external fields is below 1 nT for most of the Moon.

[35] In section 4, the global distribution of anomalies presented in Figure 7 and the applications of this data are discussed.

## 4. Discussion

### 4.1. General Distribution of Crustal Magnetization

[36] Consistent with previous studies we find that the largest distributions of crustal anomalies are located antipodal to the Crisium, Serenitatis, Imbrium, and Orientale basins. There is a tendency for the strongest anomalies antipodal to Imbrium to lie along the edge of the pre-Nectarian South Pole–Aitken (SPA) basin (see Figure 7) [Purucker *et al.*, 2006; Hood and Artemieva, 2008]. SPA is clear on the Clementine maps (Figure 7 background) as a dark circular feature in the southern farside. This result is highlighted by the 40 km constant altitude plot (Figure 7b), only the strongest anomalies persist at 40 km and the anomalies antipodal to Imbrium clearly fall along the northwest edge of SPA. The complex fields associated with the anomaly cluster antipodal to Imbrium means it is less straightforward to identify short-wavelength external fields in the vicinity of the anomaly cluster. This must be considered before quantitative analysis can be carried out for these anomalies.

[37] In addition to the anomaly clusters, we also map the previously studied isolated anomalies at Reiner Gamma, Rima Sirsalis, Descartes, and Airy [e.g., Hood, 1980; Hood *et al.*, 2001; Halekas *et al.*, 2001]. The Descartes anomaly is the strongest isolated anomaly on the Moon. Previous LP-MAG studies of the Descartes anomaly [Richmond *et al.*, 2003] were limited due to partial coverage of the anomaly. The new processing reported here provides multiple sets of complete coverage of the anomaly at Descartes, a significant improvement over previously available LP-MAG data.

### 4.2. Correlative Studies of Basin Magnetization

[38] Statistical correlation studies have previously been carried out for the basin antipode anomalies in an effort to identify likely source terranes [Hood and Williams, 1989; Richmond *et al.*, 2005]. Results indicated that for the anomaly clusters antipodal to Imbrium and Orientale the sources are likely to be basin ejecta or seismically modified terranes associated with the antipodal basins. Coverage limits in both studies meant it was not possible to consider the Serenitatis antipode or the full distribution of magnetization near Mare Marginis antipodal to Orientale.

[39] The improved coverage reported here can be used to study larger areas. New preliminary estimates of normalized occurrence rates have therefore been determined. Specifi-

cally, the area from 50 to 120°E and 40°N to 40°S near Mare Marginis has been considered. This area has a wide distribution of unusual antipode terrane and high-albedo swirls [Wilhelms and El-Baz, 1977]. The possible association of both of these units with regions of high field strength is of particular interest, with applications to both the origin of the magnetization and the nature of the interaction between the crustal magnetic fields and solar wind [e.g., Richmond *et al.*, 2005]. The area of interest has been subdivided into 1° by 1° cells with each cell assigned two values: One describing the average magnetic field magnitude at 30 km altitude and the other the main geological unit within each cell. Occurrence rates have then been calculated by dividing the number of cells of a particular geologic unit within a given field increment by the total number of cells of that type on the geologic map. The occurrence rates have then been normalized by dividing the result by the value obtained when all cells in the area are allowed. A normalized occurrence rate (NOR) greater than 1 indicates a greater than average number of cells within a given field increment, while an NOR less than 1 indicates a lower than average number of cells in a given field increment.

[40] NORs for the high-albedo swirls and unusual antipode terrane are presented in Figure 9. The unusual antipode terrane was found to correlate with regions of strong crustal magnetization (black in Figure 9). This indicates that the antipode terrane is a likely source of the magnetization. The origin of the unusual terrane is the subject of some debate, with both an ejecta and seismic origin proposed [Moore *et al.*, 1974; Schultz and Gault, 1975; Hood and Artemieva, 2008]. However, in both cases the terrane is argued to be related directly to the formation of the antipodal basins. Consequently, the results in Figure 9, calculated using the improved coverage reported here, supports the hypothesis that the Mare Marginis anomaly cluster formed in association with the Orientale basin [e.g., Hood and Williams, 1989].

[41] The results presented in Figure 9 also indicate a statistical correlation between crustal magnetization and albedo, consistent with previous studies. If the albedo is the result of surface scouring due to an external process such as a cometary [e.g., Gold and Soter, 1976] or meteoroid swarm [e.g., Starukhina and Shkuratov, 2004] impact, it is highly unlikely that the basin-related terrane would also be preferentially magnetized. Consequently, the statistical correlation between high-albedo swirls and regions of high field strength, combined with the correlation between basin-related terranes and regions of high field strength [Hood and Williams, 1989; Richmond *et al.*, 2005] (Figure 9), indicate that the swirls are more likely to be due to surface shielding by Imbrian-aged magnetic anomalies. In this process, the magnetic anomalies deflect the solar wind and prevent the regolith from reaching optical maturity, resulting in the observed high-albedo regions [e.g., Hood and Schubert, 1980].

### 4.3. Basin Magnetization

[42] In this study, we map weak anomalies at Crisium (15°N, 60°E) and Moscoviense (25°N, 150°E) with the LP-MAG data for the first time. These are among the weakest anomalies on the new map, and are below the magnitude of remaining external fields at 40 km. While weak, the

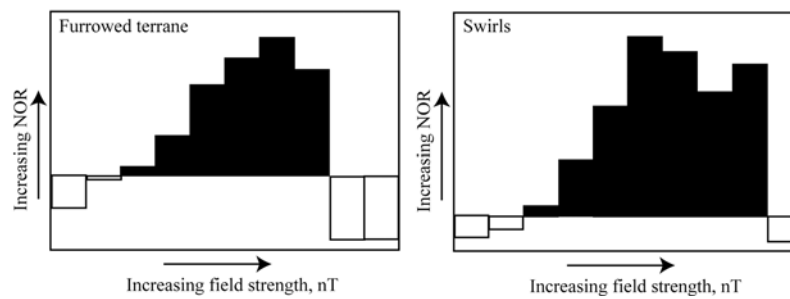


**Figure 9.** Normalized occurrence rates (NORs) for the area from 50 to 120°E and 40°N to 40°S, near Mare Marginis at the Orientale antipode. NORs greater than 1 (black) indicate a higher than average correlation, while values lower than 1 (white) indicate a lower than average correlation. Results are shown for the furrowed terrane and high-albedo swirls.

mapping of these anomalies in the LP-MAG record is potentially useful. Weak crustal fields have been detected in the LP-ER data that may be associated with remanent magnetization acquired during basin formation [Halekas *et al.*, 2003]. The anomalies at Crisium and Moscoviense were among the strongest of the weak basin anomalies identified by Halekas *et al.* [2003]. If the anomalies result from magnetization of the basins in the presence of a core dynamo field, the vector LP-MAG measurements have the potential to yield information on the direction of magnetization of the source materials, and therefore provide insight into the possible existence of a former core dynamo.

[43] However, it is notable that both of these anomalies may have an alternative explanation. Crisium is located just to the west of the Orientale antipode anomaly cluster at Mare Marginis. It has been shown [Richmond *et al.*, 2005] that an unusual furrowed terrane in the vicinity of Mare Marginis correlates statistically with regions of high field strength, a result supported by analysis of the improved coverage reported here (Figure 9). The most probable explanation for the furrowed terrane is that it is directly associated with the formation of Orientale, resulting from either converging seismic waves [Schultz and Gault, 1975] or a concentration of basin ejecta [Moore *et al.*, 1974]. The furrowed terrane extends from south of Crisium across the Mare Marginis region [Wilhelms and El-Baz, 1977], and seismic modification or basin ejecta due to Orientale may play a role in the anomalies at Crisium. It is notable that unlike the other basin anomalies reported by Halekas *et al.* [2003], the Crisium anomaly is not centered over the middle of Crisium, an observation supported by the analysis presented here (see Figure 7a). Instead, the Crisium anomaly has two peaks in the field strength, one over the southern part of the basin, the other over the northern part. This is in contrast to what we would expect if the magnetization results from basin magnetization at the time Crisium formed, and, of the magnetized basins reported by Halekas *et al.* [2003], Crisium was the only one for which the central region was not magnetized. This may argue in support of the idea that the antipodal effects resulting from the formation of Orientale could have modified any preexisting magnetization at Crisium.

[44] The magnetization at Moscoviense is interesting for two reasons. First, as discussed previously the largest distributions of crustal magnetization are in the areas

antipodal to Crisium, Serenitatis, Imbrium and Orientale, four similarly aged basins. The Humorum basin is the next oldest [Wilhelms, 1987], and mapping of the crustal field at the antipode of that basin may provide improved understanding of the nature of the magnetizing field that gave rise to the antipode clusters. The Humorum antipode is located at  $\sim 22^\circ\text{N}$ ,  $142^\circ\text{E}$  (southwestern Moscoviense), an area for which LP-MAG coverage was not previously available. Second, unusual high-albedo swirls of the Reiner Gamma-type have been mapped at Mare Moscoviense [Hughes *et al.*, 2006]. As a result, while the Moscoviense/Humorum antipode anomaly is very weak, it directly relates to basin and/or basin antipode effects, and the nature of the association between albedo and magnetization.

#### 4.4. Other Anomalies

[45] A number of previously unreported isolated anomalies have been mapped, including (1) a relatively strong anomaly at  $\sim 30^\circ\text{S}$ ,  $90^\circ\text{E}$  near the crater Abel (a series of passes over the anomaly are shown in Figure 4); (2) at  $\sim 10^\circ\text{S}$ ,  $280^\circ\text{E}$  near the crater Hartwig; and (3) at  $\sim 40^\circ\text{S}$ ,  $5^\circ\text{E}$  near Stöfler. Identification of possible source materials for these anomalies is problematic due to the complex geology in those areas. For example, the region near Abel is dominated by Imbrian-aged cratering units, Imbrian-aged mare units, and older Nectarian/pre-Nectarian terranes [Wilhelms and El-Baz, 1977]. However, it is interesting to note that for the anomaly near Abel high-albedo markings have not been mapped [Wilhelms and El-Baz, 1977]. While it is possible that swirls are present and difficult to map due to the variable terrane in the area (swirl markings are more prominent on the darker mare terranes), the lack of clear swirl markings raises interesting questions on the apparent association between magnetization and albedo reported elsewhere. Future work on this anomaly will use the Clementine albedo map to look for evidence of unusual high albedo at this location.

[46] A relatively weak series of anomalies has been mapped near  $\sim 60^\circ\text{E}$ ,  $45^\circ\text{S}$ . Only the strongest anomalies can be seen on Figure 7a. The location of these anomalies is interesting. This region is southeast of the Nectaris basin and there are several linear crater chains in this area (e.g., Vallis Snellius and Vallis Rheito), which have been interpreted to be crater chains related to the formation of Nectaris [e.g., Wilhelms, 1987].

#### 4.5. Application to Quantitative Studies of Anomaly Source Properties and Solar Wind Interaction

[47] The global map in Figure 7 is a two-dimensionally smoothed plot and as such is of primary use in understanding the general distribution of crustal magnetization. However, the pass data used to produce the map are of sufficiently high quality that they can be used for quantitative analysis of source properties. This is of particular value for the calculation of directions of magnetization. The possible existence of a former lunar core dynamo continues to be the subject of debate [e.g., *Stegman et al.*, 2003]. Estimates of paleopole positions for different lunar crustal anomalies are necessary if that issue is to be resolved. The nightside data when the Moon was in the solar wind and passes when the spacecraft was in the geomagnetic tail (Table 2) are most useful for quantitative studies.

[48] As discussed previously, dayside solar wind passes measure the field resulting from the interaction between the solar wind and the crustal anomalies (see section 3.1.4). These passes do not provide usable quantitative data for the modeling of source properties, and were not used in the production of the global map in Figure 7. However, comparisons of isolated anomalies under quiet external conditions and when exposed to the solar wind have the potential to provide insight into the way in which the anomalies interact with the incident solar wind ion bombardment [e.g., *Kurata et al.*, 2005]. Improved understanding of this interaction may have implications to the understanding of the origin of high-albedo swirls. Consequently, the dayside, solar wind passes identified in Table 2 are potentially useful for the investigation of the interaction between the solar wind and crustal anomalies.

#### 5. Conclusions

[49] We have revisited the low-altitude LP-MAG data and identified 2360 complete or partial passes that are sufficiently low in external fields to be used to study the global, vector lunar crustal magnetic field. 329 passes have been selected which provide the best coverage and those data have been used to produce a global, constant altitude map of the vector magnetic field. The passes used to produce the global map show crustal sources that repeat under different plasma conditions and in different months, showing that the map presents genuine crustal sources. Results are consistent with previous studies, with the largest distributions of anomalies located antipodal to the Crisium, Serenitatis, Imbrium and Orientale basins. Isolated anomalies are identified at Reiner Gamma, Rima Sirsalis, Descartes and Airy. In addition, a previously unreported, strong isolated anomaly has been identified near the crater Abel. A series of weaker anomalies has been mapped in an area dominated by crater chains associated with the formation of Nectaris. Two of the weakest anomalies identified are located at Mare Crisium and Mare Moscovense. Previous studies using the LP-ER data have suggested these anomalies may be due to magnetization acquired at the time the basins formed. The coverage reported here provides the first vector measurements of these anomalies and the next step is to carry out forward modeling to investigate the direction of magnetization for these two basin anomalies to determine whether they formed in the presence of a core dynamo field. Future

work with the new data set will focus on studying in more detail the association between albedo, geology and magnetization using modeling methods. In addition, the data selection method used has yielded multiple sets of coverage of anomalies under different plasma conditions. These data will be used to study further the way in which the crustal anomalies interact with the solar wind.

[50] **Acknowledgments.** Processing and mapping of the Lunar Prospector magnetometer data is supported by the NASA Discovery Data Analysis Program. Reviews by Jasper Halekas and Mike Purucker contributed significantly to the improvement of the manuscript. This is PSI contribution 424.

#### References

- Coleman, P. J., C. T. Russell, L. R. Sharp, and G. Schubert (1972), Preliminary mapping of the lunar magnetic field, *Phys. Earth Planet. Inter.*, **6**, 167–174.
- Fuller, M., and S. M. Cisowski (1987), Lunar paleomagnetism, in *Geomagnetism*, edited by J. Jacobs, pp. 307–455, Academic, Orlando, Fla.
- Gold, T., and S. Soter (1976), Cometary impact and the magnetization of the Moon, *Planet. Space Sci.*, **24**, 45–54.
- Halekas, J. S., D. L. Mitchell, R. P. Lin, S. Frey, L. L. Hood, M. H. Acuña, and A. B. Binder (2001), Mapping of crustal magnetic anomalies on the Lunar near side by the Lunar Prospector electron reflectometer, *J. Geophys. Res.*, **106**, 27,841–27,852.
- Halekas, J. S., R. P. Lin, and D. L. Mitchell (2003), Magnetic fields of lunar multi-ring impact basins, *Meteor. Planet. Sci.*, **38**, 565–578.
- Halekas, J. S., S. D. Bale, D. L. Mitchell, and R. P. Lin (2005), Electrons and magnetic fields in the lunar plasma wake, *J. Geophys. Res.*, **110**, A07222, doi:10.1029/2004JA010991.
- Halekas, J. S., D. A. Brain, D. L. Mitchell, R. P. Lin, and L. Harrison (2006), On the occurrence of magnetic enhancements caused by solar wind interaction with lunar crustal fields, *Geophys. Res. Lett.*, **33**, L08106, doi:10.1029/2006GL025931.
- Harnett, E. M., and R. M. Winglee (2003), 2.5-D fluid simulations of the solar wind interacting with multiple dipoles on the surface of the Moon, *J. Geophys. Res.*, **108**(A2), 1088, doi:10.1029/2002JA009617.
- Hood, L. L. (1980), Bulk magnetization properties of the Fra Mauro and Reiner Gamma formations, *Proc. Lunar Planet. Sci. Conf.*, **11th**, 1879–1896.
- Hood, L. L., and N. A. Artemieva (2008), Antipodal effects of lunar basin-forming impacts: Initial 3D simulations and comparisons with observations, *Icarus*, in press, doi:10.1016/j.icarus.2007.08.023.
- Hood, L. L., and Z. Huang (1991), Formation of magnetic anomalies antipodal to lunar impact basins: Two-dimensional model calculations, *J. Geophys. Res.*, **96**, 9837–9846.
- Hood, L. L., and G. Schubert (1980), Lunar magnetic anomalies and surface optical properties, *Science*, **208**, 49–51.
- Hood, L. L., and A. Vickery (1984), Magnetic field amplification and generation in hypervelocity meteoroid impacts with application to Lunar paleomagnetism, *Proc. Lunar Planet. Sci. Conf. 15th*, Part 1, *J. Geophys. Res.*, **89**, suppl., C211–C223.
- Hood, L. L., and C. R. Williams (1989), The Lunar swirls: Distribution and possible origins, *Proc. Lunar Planet. Sci. Conf.*, **19th**, 99–113.
- Hood, L. L., C. T. Russell, and P. J. Coleman Jr. (1981), Contour maps of the lunar remanent magnetic fields, *J. Geophys. Res.*, **86**, 1055–1069.
- Hood, L. L., A. Zakharian, J. Halekas, D. L. Mitchell, R. P. Lin, M. H. Acuña, and A. B. Binder (2001), Initial mapping and interpretation of lunar crustal magnetic anomalies using lunar prospector magnetometer data, *J. Geophys. Res.*, **106**, 27,825–27,839.
- Housley, R. M. (1977), Solar wind and micrometeorite effects in the lunar regolith, *Philos. Trans. R. Soc. London, Ser. A*, **285**, 363–370.
- Hughes, C. G., D. T. Blewett, B. R. Hawke, and N. C. Richmond (2006), Optical maturity and magnetic studies of lunar swirls, *Lunar Planet. Sci. Conf. [CD-ROM]*, **XXXVII**, Abstract 1230.
- Kurata, M., H. Tsunakawa, Y. Saito, H. Shibuya, M. Matsushima, and H. Shimizu (2005), Mini-magnetosphere over the Reiner Gamma magnetic anomaly region on the Moon, *Geophys. Res. Lett.*, **32**, L24205, doi:10.1029/2005GL024097.
- Lin, R. P., K. A. Anderson, and L. L. Hood (1988), Lunar surface magnetic field concentrations antipodal to young large impact basins, *Icarus*, **74**, 529–541.
- Lin, R. P., D. L. Mitchell, D. W. Curtis, K. A. Anderson, C. W. Carlson, J. McFadden, M. H. Acuña, L. L. Hood, and A. B. Binder (1998), Lunar surface magnetic fields and their interaction with the solar wind: Results from Lunar Prospector, *Science*, **281**, 1480–1484.



- Mitchell, D. L., J. S. Halekas, R. P. Lin, S. Frey, L. L. Hood, M. H. Acuña, and A. Binder (2008), Global mapping of lunar crustal magnetic fields by Lunar Prospector, *Icarus*, in press.
- Moore, H. J., C. A. Hodges, and D. H. Scott (1974), Multiringed basins-illustrated by Orientale and associated features, *Geochim. Cosmochim. Acta*, 1, Suppl. 1, 71–100.
- Nakagawa, T., Y. Takahashi, and M. Iizima (2003), Geotail observation of upstream ULF waves associated with the lunar wake, *Earth Planets Space*, 55, 569–580.
- Nicholas, J. B., M. E. Purucker, and T. J. Sabaka (2007), Age spot or youthful marking: Origin of Reiner Gamma, *Geophys. Res. Lett.*, 34, L02205, doi:10.1029/2006GL027794.
- Pieters, C., E. Fischer, O. Rode, and A. Basu (1993), Optical effects of space weathering: The role of the finest fraction, *J. Geophys. Res.*, 98, 20,817–20,824.
- Purucker, M. E., T. J. Sabaka, and R. A. Langel (1996), Conjugate gradient analysis: a new tool for studying spacecraft magnetic data sets, *Geophys. Res. Lett.*, 23, 507–510.
- Purucker, M. E., T. J. Sabaka, J. Halekas, N. Olsen, N. Tsyganenko, and L. L. Hood (2006), The lunar magnetic field environment: Interpretation of new maps of the internal and external fields, *Lunar Planet. Sci. Conf. [CD-ROM]*, XXXVI, Abstract 1933.
- Richmond, N. C., L. L. Hood, J. S. Halekas, D. L. Mitchell, R. P. Lin, M. Acuña, and A. B. Binder (2003), Correlation of a strong lunar magnetic anomaly with a high-albedo region of the Descartes mountains, *Geophys. Res. Lett.*, 30(7), 1395, doi:10.1029/2003GL016938.
- Richmond, N. C., L. L. Hood, D. L. Mitchell, R. P. Lin, M. H. Acuña, and A. B. Binder (2005), Correlations between magnetic anomalies and surface geology antipodal to lunar impact basins, *J. Geophys. Res.*, 110, E05011, doi:10.1029/2005JE002405.
- Russell, C. T., P. J. Coleman Jr., B. K. Fleming, L. Hilburn, G. Ioannidis, B. R. Lichtenstein, and G. Schubert (1975), The fine scale lunar magnetic field, *Proc. Lunar Sci. Conf.*, 6th, 2955–2969.
- Schultz, P. H., and D. E. Gault (1975), Seismic effects from major basin formations on the Moon and Mercury, *Moon*, 12, 159–177.
- Schultz, P. H., and L. J. Srnka (1980), Cometary collisions with the Moon and Mercury, *Nature*, 284, 22–26.
- Starukhina, L. V. (2007), Meteorite swarm encounters as a source of magnetic anomalies on the lunar and Mercurian surfaces, *Lunar Planet. Science Conf. [CD-ROM]*, XXXVIII, Abstract 1299.
- Starukhina, L. V., and Y. G. Shkuratov (2004), Swirls on the Moon and Mercury: meteoroid swarm encounters as a formation mechanism, *Icarus*, 167, 136–147.
- Stegman, D. R., A. M. Jellinek, S. A. Zatman, J. R. Baumgardner, and M. A. Richards (2003), An early lunar core dynamo driven by thermochemical mantle convection, *Nature*, 421, 143–146.
- Strangway, D. W., H. Sharpe, W. Gose, and G. Pearce (1973), Lunar magnetic anomalies and the Cayley Formation, *Nature*, 246, 112–114.
- Taylor, L. A., C. M. Pieters, L. P. Keller, R. V. Morris, and D. S. McKay (2001), Lunar mare soils: Space weathering and the major effects of surface-correlated nanophase Fe, *J. Geophys. Res.*, 106, 27,985–27,999.
- Wilhelms, D. E. (1987), The geologic history of the Moon, *U.S. Geol. Surv. Prof. Pap.*, 1348.
- Wilhelms, D., and F. El-Baz (1977), Geologic map of the east side of the Moon, *U.S. Geol. Surv. Misc. Geol. Invest. Map*, I-948.

---

L. L. Hood and N. C. Richmond, Lunar and Planetary Laboratory, University of Arizona, Kuiper Space Sciences Building, 1629 East University Boulevard, Tucson, AZ 85721, USA. (nic@lpl.arizona.edu)